

Neural Ordinary Differential Equations for Mapping the Magnetic QCD Phase Diagram via Holography

Rong-Gen Cai^{b,c,d,e}, Song He^{a,b,c,f}, Li Li^{d,e,g}, Hong-An Zeng^a

^aCenter for Theoretical Physics and College of Physics, Jilin University,
Changchun 130012, People's Republic of China

^bInstitute of Fundamental Physics and Quantum Technology,
Ningbo University, Ningbo, Zhejiang 315211, China

^cSchool of Physical Science and Technology, Ningbo University, Ningbo, 315211, China

^dCAS Key Laboratory of Theoretical Physics, Institute of Theoretical Physics,
Chinese Academy of Sciences, Beijing 100190, China

^eSchool of Fundamental Physics and Mathematical Sciences,

Hangzhou Institute for Advanced Study, UCAS, Hangzhou 310024, China

^fMax Planck Institute for Gravitational Physics (Albert Einstein Institute),
Am Mühlenberg 1, 14476 Golm, Germany and

^gSchool of Physical Sciences, University of Chinese Academy of Sciences, Beijing 100049, China.*

The QCD phase diagram is crucial for understanding strongly interacting matter under extreme conditions, with major implications for cosmology, neutron stars, and heavy-ion collisions. We present a novel holographic QCD model utilizing neural ordinary differential equations (ODEs) to map the QCD phase diagram under magnetic field B , baryon chemical potential μ_B , and temperature T . By solving the inverse problem of constructing the gravitational theory from Lattice QCD data, we reveal an unprecedentedly rich phase structure at finite B , including discovering multiple critical endpoints (CEPs) under strong magnetic fields. Specifically, for $B = 1.618 \text{ GeV}^2 = 2.592 \times 10^{19} \text{ Gauss}$, we identify two distinct CEPs at $(T_C = 87.3 \text{ MeV}, \mu_C = 115.9 \text{ MeV})$ and $(T_C = 78.9 \text{ MeV}, \mu_C = 244.0 \text{ MeV})$. Notably, the critical exponents vary depending on the CEP's location. These findings significantly advance our understanding of the QCD phase structure and provide concrete predictions for experimental validation at upcoming facilities such as FAIR, JPARC-HI, and NICA.

I. INTRODUCTION

Quantum Chromodynamics (QCD), the theory of strong interactions, governs quark and gluon behavior under extreme conditions, underpinning high-energy physics, astrophysics, and cosmology. The QCD phase diagram, which maps transitions between the deconfined quark-gluon plasma and hadronic matter, is central to understanding phenomena in non-central heavy-ion collisions, neutron stars, and the early universe [1–3]. The global structure of the QCD phase diagram, spanning temperature (T), baryon chemical potential (μ_B), and magnetic field (B), remains poorly understood [4]. At low μ_B and $B = 0$, QCD matter undergoes a smooth crossover, while at high μ_B , a first-order phase transition occurs. Locating the critical endpoint (CEP) separating these regimes is a primary goal of heavy-ion collision experiments [5, 6]. Magnetic fields, generated in non-central heavy-ion collisions and present in astrophysical objects like magnetars, significantly influence the QCD equation of state. Strong magnetic fields modify the critical temperature, induce novel phases, and play a key role in shaping the QCD phase structure [4], making B an essential factor in searching CEP experimentally [7][8][9]. Exploring the magnetic QCD phase structure remains a significant challenge.

With substantial progress, current non-perturbative approaches to studying the QCD phase diagram still face

significant challenges. As a first-principle approach, Lattice QCD encounters the well-known *sign problem* at finite baryon density, making numerical simulations at high μ_B computationally prohibitive [2]. Moreover, simulating high magnetic field configurations demands substantial computational resources, leading to limited exploration of the QCD phase structure in these regions [4]. These limitations significantly hinder our understanding of the interplay among T , μ_B , and B , particularly in the regions of the phase diagram where experimental observations are most challenging.

As a competitive approach, holography offers a computationally efficient framework to study non-perturbative QCD systems by mapping them to classical gravity [10–12]. The holographic framework has particularly effectively captured QCD dynamics at finite temperatures and densities [13–15]. Several refined models, only capturing corner of the QCD phase diagram, still fall short of quantitatively describing the full set of lattice QCD data, even for QCD equations of state [16–23]. To construct a holographic model consistent with QCD data, one must systematically explore various actions and scan the parameter space—a task akin to finding a needle in a haystack. Manual parameter tuning to fit lattice QCD data, known as the *inverse problem*, is computationally inefficient and often fails to capture the system's complexity, particularly in the multi-dimensional parameter space of T , μ_B , and B [12, 16, 24].

Neural ordinary differential equations (neural ODEs) excel in modeling complex, continuous dynamic systems by optimizing over infinite-dimensional parameter spaces with adaptive precision. In this work, we leverage neural ODEs in holography to address these challenges, offering a data-driven mechanism that is different from traditional machine learning methods [25–29]. This innovative approach captures the intricate dependencies of thermodynamic quantities on T , μ_B , and B with unprecedented accuracy and flexibility [30].

These advantages allow our approach to a concrete global structure of the phase diagram and uncover unprecedented novel features of the QCD phase structure, such as multiple CEPs and their associated critical behaviors, which were previously never identified. In particular, for sufficiently large $B = 1.618 \text{ GeV}^2 = 2.592 \times 10^{19}$ Gauss, the T - μ_B plane exhibits two CEPs, a feature exceeding prior expectations. Furthermore, we analyze the critical behavior near the CEPs, finding that the critical exponents satisfy scaling relations but vary based on the CEP's location. This innovative combination of machine learning and holography significantly advances our understanding of the QCD phase structure and provides new avenues for better agreement with experimental and lattice QCD results.

The article is organized as follows. We introduce the holographic model in Section II. We then describe our method for fixing the bulk theory using machine learning in Section III. The full QCD phase diagram and its key features are summarized in Section IV and Section V. We conclude and provide future directions in Section VI. In Appendix A, we additionally show the details on solving the equations of motion and the definition of thermodynamic quantities. A detailed algorithmic breakdown of the neural ODEs is included in Appendix B.

II. HOLOGRAPHIC MODEL

To capture essential QCD dynamics at finite magnetic field, temperature, and baryon chemical potential, we employ a holographic framework based on the five-dimensional gravitational theory:

$$S = \frac{1}{2\kappa_N^2} \int d^5x \sqrt{-g} \left[\mathcal{R} - \frac{1}{2} \nabla_\mu \phi \nabla^\mu \phi - \frac{Z(\phi)}{4} F_{\mu\nu} F^{\mu\nu} - \frac{\hat{Z}(\phi)}{4} \hat{F}_{\mu\nu} \hat{F}^{\mu\nu} - V(\phi) \right], \quad (1)$$

where κ_N^2 is the effective Newton constant. The metric $g_{\mu\nu}$ characterizes spacetime geometry, and the real scalar field ϕ accounts for conformal symmetry breaking. The Maxwell field A_μ with $F_{\mu\nu} = \partial_\mu A_\nu - \partial_\nu A_\mu$ introduces a finite baryon number density, while the magnetic field B is described by another Maxwell field \hat{A}_μ with $\hat{F}_{\mu\nu} = \partial_\mu \hat{A}_\nu - \partial_\nu \hat{A}_\mu$. The functions $Z(\phi)$, $\hat{Z}(\phi)$, and $V(\phi)$ that

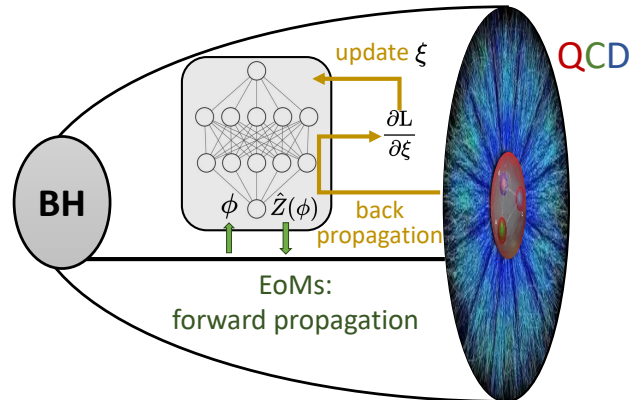


FIG. 1. Schematic of the neural ODE approach for solving the inverse problem in QCD phase diagram analysis. Initial conditions from the black hole (BH) horizon are connected to QCD boundary data via EoMs. The neural network initialized as a trial function for the coupling $\hat{Z}(\phi)$ is optimized via backpropagation to minimize the loss function L , representing the difference from lattice QCD data. Parameters ξ are optimized using gradient descent. Technical details are provided in Appendix B.

encode the non-perturbative features of our system are calibrated against lattice QCD data.

The bulk black hole solutions in Anti-de Sitter spacetime (AdS) are

$$ds^2 = -f(r)e^{-\eta(r)} dt^2 + \frac{dr^2}{f(r)} + r^2(dx^2 + dy^2 + g(r)dz^2),$$

$$\phi = \phi(r), \quad A_\mu dx^\mu = A(r)dt, \quad \hat{A}_\mu dx^\mu = \frac{B}{2}(xdy - ydx), \quad (2)$$

where r is the holographic radial coordinate with the AdS boundary located at $r \rightarrow \infty$. The blackening function $f(r)$ is vanishing at the event horizon $r = r_h$. The temperature and entropy density of the QCD system are given by the famous Hawking temperature and Bekenstein-Hawking entropy of a black hole:

$$T = \frac{1}{4\pi} f'(r_h) e^{-\eta(r_h)/2}, \quad s = \frac{2\pi}{\kappa_N^2} r_h^3, \quad (3)$$

evaluated at the black hole event horizon. Note that the magnetic field B breaks Lorentz invariance along the z -axis, leading to anisotropic pressure. Solving the bulk equations of motion (EoMs) allows us to extract thermodynamic quantities, such as the free energy density Ω , longitudinal pressure P_z , entropy density s , baryon density n_B , and magnetization M . For further details, see Appendix A. This holographic approach provides a first-principles description of QCD dynamics under extreme conditions.

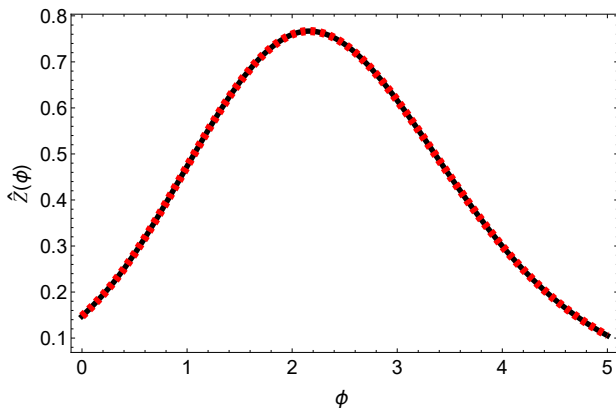


FIG. 2. The magnetic coupling $\hat{Z}(\phi)$ as a function of ϕ from machine learning. The black solid curve is the one obtained from our neural ODEs architecture, and the red dotted one from the fitting function (S25) in Appendix B.

III. NEURAL ODES

In the absence of a first-principle method to determine the coupling functions in our bottom-up model, we constrain these functionals using available lattice QCD data—a challenge known as the inverse problem. As lattice QCD data at finite B and μ_B become more abundant, manually tuning control parameters becomes impractical. Our neural ODE approach systematically explores the infinite-dimensional parameter space of the coupling functions, achieving higher precision and accuracy.

In practice, we impose boundary conditions at the ultraviolet (UV) boundary and the black hole event horizon. By solving the EoMs numerically, the neural ODE generates a trial equation of state that is iteratively optimized through backpropagation to reduce deviations from lattice QCD data. This process efficiently converges to an optimal magnetic coupling, providing a good agreement with lattice data and refining model predictions across unexplored magnetic fields and chemical potentials (see Fig. 1 for illustration). A detailed algorithmic breakdown of this methodology is included in Appendix B. We construct a (2+1)-flavor holographic QCD (hQCD) model using this neural ODE approach to achieve a precise fit with lattice QCD results [35]. A similar neural ODE-based method is applied to determine $Z(\phi)$ and $V(\phi)$ by matching to data at $B = 0$ [36, 37]. The resulting functional forms are benchmarked rigorously and agree with recent lattice simulations and experimental data [38, 39]. The profile for $\hat{Z}(\phi)$ from our neural ODEs is presented in Fig. 2. This strong non-monotonicity highlights the necessity for parameter tuning in machine learning.

Fig. 3 presents our holographic predictions for four independent thermodynamic quantities: magnetic suscep-

tibility χ^B , magnetization M , entropy density s , and longitudinal pressure p_z , compared to lattice QCD data [35]. We find good agreement across the available magnetic fields, supporting our holographic model. This is the first holographic model to achieve good agreement with lattice data for magnetic fields up to $B = 0.6 \text{ GeV}^2$. Further analysis is provided in Appendix B, showing consistency with lattice QCD results [35].

IV. QCD PHASE DIAGRAM

With the model fully established, we construct the QCD phase diagram at finite B , T , and μ_B by computing the free energy density Ω . The full phase diagram is depicted in Fig. 5. The light blue area denotes the first-order phase transition surface, dividing the quadrant into two parts: the high-temperature region corresponds to the quark-gluon plasma, while the low-temperature region corresponds to the hadron gas phase. The deep blue line in the diagram marks the location of CEP for various magnetic fields, where the first-order phase transition terminates and transitions into a smooth crossover at small chemical potentials. At $B = 0$, the phase diagram was presented in Fig. 3 of [38], where the first-order transition line terminates at $(T_C = 105 \text{ MeV}, \mu_C = 555 \text{ MeV})$. Fig. 4 shows the phase structure in the T - B plane at $\mu_B = 0$, revealing a line of first-order transitions ending at the CEP located at $(T_C = 89.6 \text{ MeV}, B = 1.6 \text{ GeV}^2)$, consistent with lattice QCD predictions [40].

Fig. 5 highlights the following three key observations [41].

1. As the magnetic field B increases up to $B = 1.764 \text{ GeV}^2$, the critical chemical potential μ_C at the CEP decreases, indicating that stronger magnetic fields shift the CEP to lower chemical potentials. This shows a significant effect of magnetic fields on the CEP location, affecting conditions in experimental settings like heavy-ion collisions.
2. The critical temperature T_C at the CEP initially decreases with increasing B , reaching a minimum before increasing again. This turning point occurs around $T = 80 \text{ MeV}$, $B = 1.6 \sim 1.7 \text{ GeV}^2$, and $\mu_B = 0.2 \sim 0.28 \text{ GeV}$. This behavior suggests complicated effects in the presence of a background magnetic field. It could be related to the inverse magnetic catalysis and magnetic catalysis reported in the literature.
3. Multiple CEPs emerge at sufficiently strong magnetic fields in the T - μ_B phase diagram, as shown in Fig. 6. A first-order phase transition occurs for $0 < \mu_B < \mu_{C1}$ and $\mu_B > \mu_{C2}$, while a crossover exists when $\mu_{C1} < \mu_B < \mu_{C2}$. As the

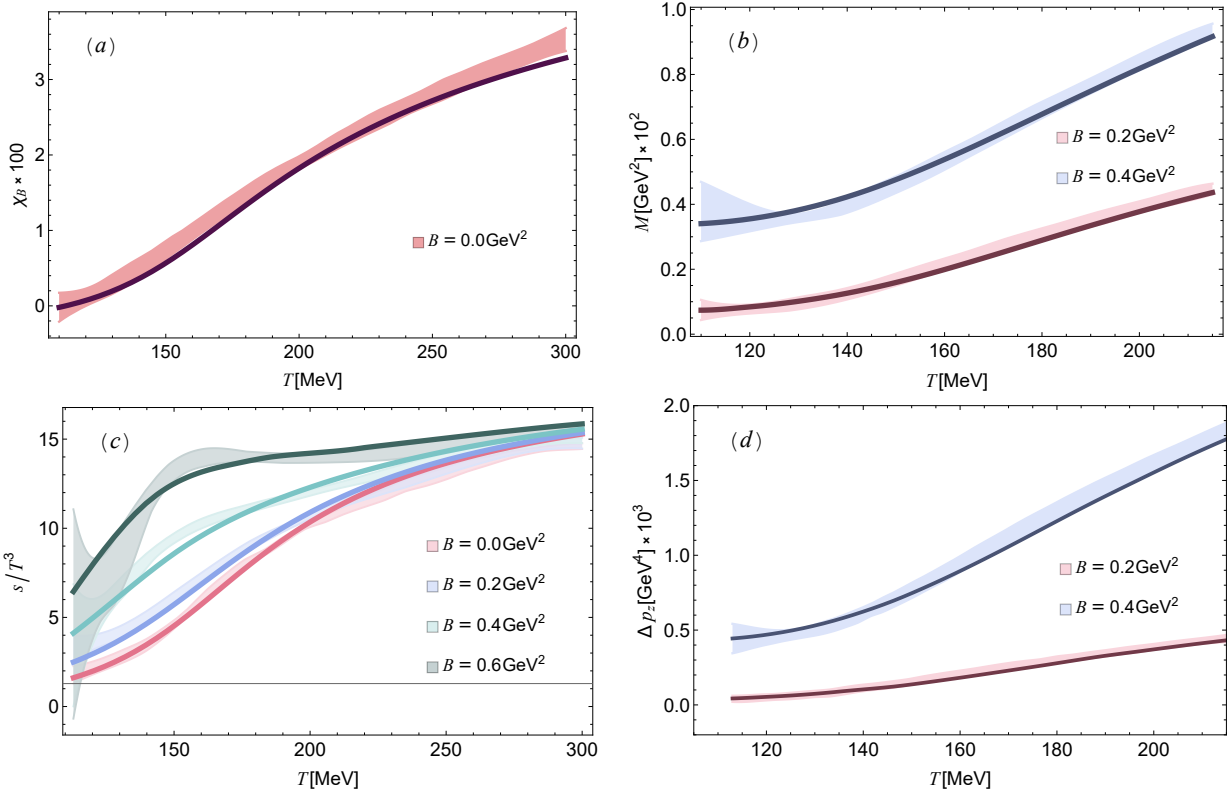


FIG. 3. Thermodynamic Quantities from Holographic QCD Model vs. Lattice Data. Temperature dependence of (a) magnetic susceptibility χ_B , (b) magnetization M , (c) entropy density s/T^3 , and (d) longitudinal pressure $\Delta p_z = p_z|_B - p_z|_{B=0}$ across magnetic fields. Shaded regions show lattice QCD estimates [35]; solid lines indicate model predictions. Here, $e = 1$, giving $B = 1 \text{ GeV}^2 = 1.602 \times 10^{19}$ Gauss.

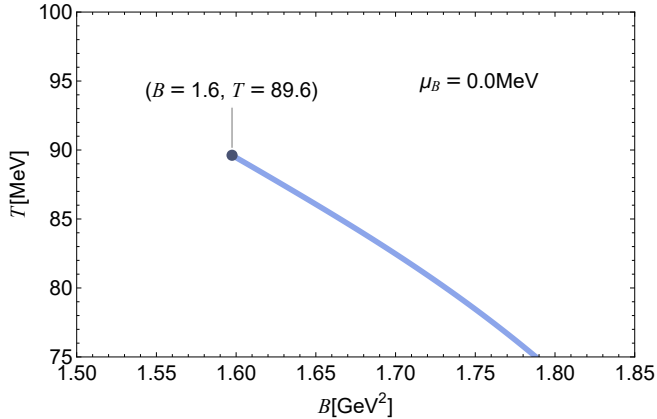


FIG. 4. The phase diagram on the B - T plane at vanishing μ_B . The blue dot denotes the CEP, and the blue line corresponds to the first-order line.

magnetic field B increases, the two CEPs, initially distinct, converge into a single point. Specifically, Fig. 6 illustrates two CEPs identified at $(T_C, \mu_C) = (87.3 \text{ MeV}, 115.9 \text{ MeV})$ and $(T_C, \mu_C) = (78.9 \text{ MeV}, 244.0 \text{ MeV})$. This result holds significant implications for heavy-ion collision experi-

ments, providing precise experimental markers for testing at FAIR, JPARC-HI, and NICA [42].

These key observations reveal a rich phase structure in a strong magnetic field and warrant further experimental verification.

V. CRITICAL EXPONENTS

Beyond mapping the phase diagram, we examine critical behavior near the CEPs via critical exponents. These exponents describe how thermodynamic quantities, such as susceptibility and specific heat, diverge near critical points, typically following power-law scaling. These exponents help identify the CEP's universality class and provide insights into QCD transitions under extreme conditions.

Four critical exponents can be directly extracted from the phase diagram of Fig. 5.

- **Critical exponent α :** The exponent α quantifies the power-law behavior of specific heat near a CEP along the axis defined as approaching the

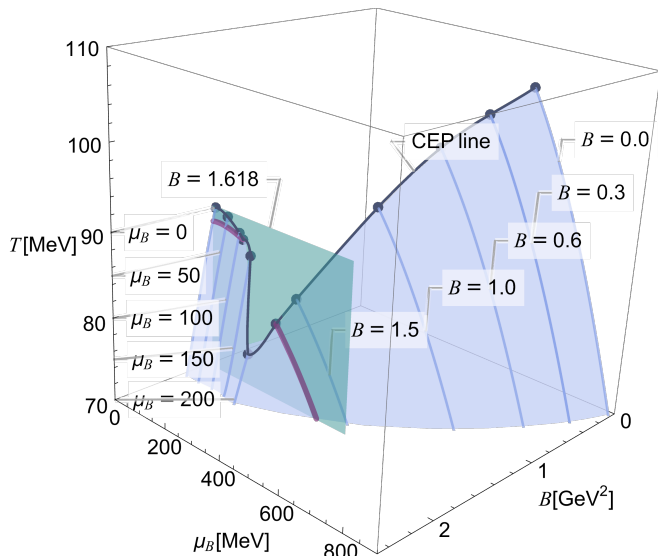


FIG. 5. QCD phase diagram at finite magnetic field B . Phase structure in temperature T , baryon chemical potential μ_B , and magnetic field B from our holographic model. The light blue surface denotes the first-order transition boundary, separating the hadronic phase from the quark-gluon plasma. The dark blue line traces the CEP trajectory, marking where the first-order transition ends in a crossover.

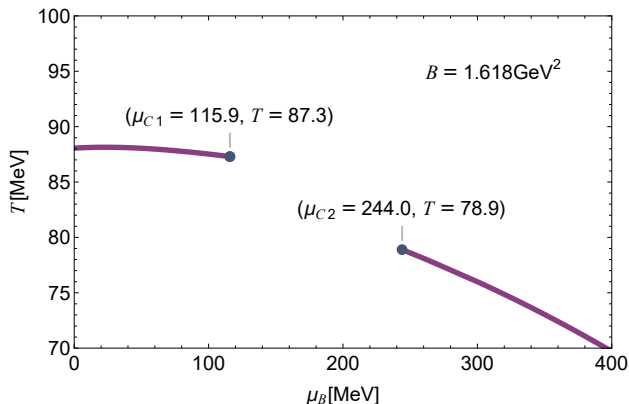


FIG. 6. QCD phase diagram in the T - μ_B plane at $B = 1.618 \text{ GeV}^2$. The purple line marks the first-order phase transition, ending at the first critical endpoint (CEP) at $\mu_{C1} = 115.9 \text{ MeV}$, where the transition becomes a crossover. A second CEP at $\mu_{C2} = 224.0 \text{ MeV}$ suggests a more complex phase structure. These findings imply that strong magnetic fields induce rich QCD phase behavior, with significant implications for heavy-ion collisions.

CEP along the tangent of the first-order line:

$$C_n = T \left(\frac{\partial s}{\partial T} \right)_{n,B} \sim |T - T_{\text{CEP}}|^{-\alpha}.$$

- **Critical exponent β :** It characterizes the discontinuity of entropy density s across the first-order

line:

$$\Delta s = s_{>} - s_{<} \sim (T_{\text{CEP}} - T)^\beta,$$

where $s_{>}$ and $s_{<}$ represent the entropy densities in the high- and low-temperature phases, respectively.

- **Critical exponent γ :** It represents the power-law behavior of baryon susceptibility with the temperature near the CEP along the first-order axis:

$$\chi_2^B = \frac{1}{T^2} \left(\frac{\partial n_B}{\partial \mu_B} \right)_{T,B} \sim |T - T_{\text{CEP}}|^{-\gamma}.$$

- **Critical exponent δ :** The definition of δ relies on the power-law relationship between entropy and chemical potential with $T = T_{\text{CEP}}$ at the critical isotherm:

$$s - s_{\text{CEP}} \sim |\mu_B - \mu_{B\text{CEP}}|^{1/\delta},$$

where s_{CEP} is the entropy density at the CEP.

Table I presents the critical exponents for the CEP at three different magnetic field values, denoted by hQCD (I, II, III) [41]. The critical exponents satisfy the scaling relations $\alpha + 2\beta + \gamma = 2$ and $\alpha + \beta(1 + \delta) = 2$, ensuring the self-consistency of our results. Although close to mean-field values, these exponents show significant deviations depending on the CEP location, particularly as B increases. Such deviations highlight the features of our holographic QCD model, which cannot be attributed to large- N effects typical in conventional holographic duality, where mean-field behavior is expected. Similar deviation happened in the holographic 2-flavor model [43], the critical exponents match those of the quantum 3D Ising model, further emphasizing the distinct nature of our approach compared to traditional large- N QCD models.

	α	β	γ	δ
Experiment	0.110-0.116	0.316-0.327	1.23-1.25	4.6-4.9
3D Ising	0.110(5)	0.325 ± 0.0015	1.2405 ± 0.0015	4.82(4)
Mean field	0	1/2	1	3
DGR model	0	0.482	0.942	3.035
hQCD(I)	0.002296	0.485518	0.9558187	3.00993
hQCD(II)	0.001694	0.50373	0.91803	2.9455
hQCD(III)	0.00917	0.3944	0.98696	3.9878

TABLE I. Critical exponents from experiments in non-QCD fluids, the full quantum 3D Ising model, mean-field (van der Waals) theory, the DGR model [14], and our (2+1)-flavor hQCD model. The hQCD (I, II, III) correspond to the critical exponents for $\mu_B = 554.66 \text{ MeV}, B = 0$ (hQCD I), $\mu_B = 501.4 \text{ MeV}, B = 0.3 \text{ GeV}^2$ (hQCD II), and $\mu_B = 0, B = 1.6 \text{ GeV}^2$ (hQCD III), respectively.

VI. CONCLUSION

We have developed a novel neural ODE framework that solves the inverse problem of constructing a holographic

QCD action from Lattice QCD data. This framework results in the first holographic model capable of capturing key thermodynamic behaviors of hot and dense QCD at finite magnetic fields. Notably, the model reveals a rich phase structure in a strong magnetic field, including non-monotonic CEP temperature behavior (Fig. 5) and multiple CEPs in the T - μ_B plane (Fig. 6), providing specific experimental markers for validation at future facilities like FAIR, JPARC-HI, and NICA [42]. Specifically for $B = 1.618\text{GeV}^2$, we identified the first CEP at $(T_C = 87.3, \text{MeV}, \mu_C = 115.9, \text{MeV})$, and a second CEP at $(T_C = 78.9, \text{MeV}, \mu_C = 244.0, \text{MeV})$. These results suggest a richer phase structure in QCD than previously anticipated. Furthermore, we have determined critical exponents that depend on the location of CEPs, offering valuable insights for experimental studies in regions accessible to RHIC and LHC. Experimental observables, such as baryon number or magnetization fluctuations, could directly test these predictions in current experiments, e.g. RHIC [7], the STAR fixed target program (FXT), and future experiments [42].

Our work has established a fruitful connection between high-energy nuclear physics, gravity, and machine learning. We have discovered previously unexplored structures of the QCD phase diagram, providing a deeper understanding of QCD matter in extreme environments. Future research should extend the model to bridge gaps between theoretical predictions and experimental findings across energy scales. This includes incorporating isospin asymmetry, which is relevant for neutron stars, and rotational effects, critical for understanding dynamics in rapidly spinning neutron stars and heavy-ion collisions. Extending the model to non-equilibrium scenarios could also provide insights into the real-time dynamics of phase transitions, capturing rapid changes in temperature, density, and magnetic field during heavy-ion collisions. Applying our findings to neutron stars and early universe conditions, where understanding the equation of state for strongly interacting QCD matter under varying magnetic fields is crucial, presents another promising direction for future research.

ACKNOWLEDGMENTS

We thank Heng-Tong Ding, Matti Järvinen, Elias Kiritsis, Zhibin Li, Xiaofeng Luo, Yi-Bo Yang, Danning Li, Javier Subils, Ling-Xiao Wang, and Yuan-Xu Wang for stimulating discussions. This work is supported in part by the National Key Research and Development Program of China Grants No.2020YFC2201501 and No.2020YFC2201502, in part by the National Natural Science Foundation of China Grants No.12075101, No.12047569, No.12122513, No.12075298, No.11991052, No.12235016 and No.12047503. S.H. would also like to express appreciation for the financial support from the

Max Planck Partner Group.

Appendix A: Equations of motion and thermodynamics

By varying the action (1), the equations of motion (EoMs) can be obtained:

$$\begin{aligned} \nabla_\mu \nabla^\mu \phi - \frac{\partial_\phi Z}{4} F_{\mu\nu} F^{\mu\nu} - \frac{\partial_\phi \hat{Z}}{4} \hat{F}_{\mu\nu} \hat{F}^{\mu\nu} - \partial_\phi V &= 0 \\ \nabla^\nu (Z F_{\nu\mu}) &= 0 \\ \nabla^\nu (\hat{Z} \hat{F}_{\nu\mu}) &= 0 \\ R_{\mu\nu} - \frac{1}{2} R g_{\mu\nu} &= \frac{1}{2} \nabla_\mu \phi \nabla_\nu \phi + \frac{Z}{2} F_{\mu\rho} F_\nu^\rho + \frac{\hat{Z}}{2} \hat{F}_{\mu\rho} \hat{F}_\nu^\rho \\ &+ \frac{1}{2} \left(-\frac{1}{2} \nabla_\mu \phi \nabla^\mu \phi - \frac{Z}{4} F_{\mu\nu} F^{\mu\nu} - \frac{\hat{Z}}{4} \hat{F}_{\mu\nu} \hat{F}^{\mu\nu} - V \right) g_{\mu\nu}. \end{aligned} \quad (\text{S1})$$

Substituting the ansatz (2) into (S1) gives six equations:

$$\begin{aligned} \phi''(r) + \left(\frac{f'(r)}{f(r)} + \frac{1}{2} \left(\frac{6}{r} + \frac{g'(r)}{g(r)} - \eta'(r) \right) \right) \phi'(r) \\ - \frac{V'(\phi) + \frac{e^{\eta(r)} A'(r)^2 Z'(\phi(r))}{2f(r)} - \frac{B^2 \hat{Z}'(\phi)}{2r^4 f(r)}}{f(r)} = 0, \\ A''(r) + \frac{1}{2} A'(r) \left(\frac{6}{r} + \frac{g'(r)}{g(r)} + \eta'(r) + \frac{2Z'(\phi)\phi'(r)}{Z(\phi)} \right) = 0, \\ \eta'(r) + \frac{-r^3(f(r) + rf'(r))g'(r)}{r^3 f(r)(3g(r) + rg'(r))} \\ + \frac{g(r) \left(B^2 \hat{Z}(\phi) + r^4 f(r) \phi'(r)^2 \right)}{r^3 f(r)(3g(r) + rg'(r))} = 0, \\ f'(r) + \frac{1}{2} f(r) \left(\frac{4}{r} + \frac{g'(r)}{g(r)} - \eta'(r) \right) + \frac{1}{3} r V(\phi) + \frac{B^2 \hat{Z}(\phi)}{3r^3} \\ + \frac{1}{6} e^{\eta(r)} r \hat{Z}(\phi) A'(r)^2 = 0, \\ g''(r) - \frac{g'(r)^2}{2g(r)} + g'(r) \left(\frac{2}{r} + \frac{\eta'(r)}{2} \right) \\ + g(r) \left(\frac{3\eta'(r)}{r} + \phi'(r)^2 \right) = 0, \end{aligned} \quad (\text{S2})$$

where five of them are independent.

The form of $V(\phi)$ and $Z(\phi)$ is taken from [38].

$$\begin{aligned} V(\phi) &= -12 \cosh[c_1 \phi] + (6c_1^2 - \frac{3}{2}) \phi^2 + c_2 \phi^6, \\ Z(\phi) &= \frac{1}{1 + c_3} \text{sech}[c_4 \phi^3] + \frac{c_3}{1 + c_3} e^{-c_5 \phi}. \end{aligned} \quad (\text{S3})$$

Expansion at the UV boundary $r \rightarrow \infty$ yields

$$\begin{aligned}
\phi(r) &= \frac{\phi_s}{r} + \frac{(\phi_v + \frac{1}{6}(-1 + 6c_1^4)\phi_s^3 \ln[r])}{r^3} + \frac{B^2 \hat{Z}'(0)}{6r^4} + \dots, \\
g(r) &= 1 + \frac{g_4 - \frac{1}{4}B^2 \ln[r] \hat{Z}(0)}{r^4} + \frac{B^2 \phi_s \hat{Z}'(0)}{5r^5} + \dots, \\
\eta(r) &= 1 + \frac{\phi_s^2}{6r^2} + \frac{g_4}{r^4} + \frac{\left((1 - 6c_1^4)\phi_s^4 + 72\phi_s \phi_v + 12B^2 \hat{Z}(0)\right)}{144r^4} \\
&\quad + \frac{1}{12} \frac{\ln[r] \left(-((1 - 6c_1^4)\phi_s^4) - 3B^2 \hat{Z}(0)\right)}{r^4} \\
&\quad + \frac{16B^2 \phi_s \hat{Z}'(0)}{45r^5} + \dots, \\
A(r) &= \mu_B - \frac{2\kappa_N^2 n_B}{2r^2} + \frac{2\kappa_N^2 n_B \phi_s Z'(0)}{3r^3 Z(0)} \\
&\quad + \frac{2\kappa_N^2 n_B \phi_s^2 (Z(0)^2 - 12Z'(0)^2 + 6Z(0)Z''(0))}{48r^4 Z(0)^2} + \dots,
\end{aligned} \tag{S4}$$

where we have taken the normalization of the spacetime coordinates at the boundary such that $\eta(r \rightarrow \infty) = 0$ and $g(r \rightarrow \infty) = 1$. Expansion at the event horizon $r = r_h$ gives

$$\begin{aligned}
f &= f_h(r - r_h) + \dots, \\
\eta &= \eta_h + \eta_1(r - r_h) + \dots, \\
A &= A_h(r - r_h) + \dots, \\
\phi &= \phi_h + \phi_1(r - r_h) + \dots, \\
g &= g_h + g_1(r - r_h) + \dots.
\end{aligned} \tag{S5}$$

After substituting (S5) into the EoMs (S2), one finds five independent coefficients $(r_h, A_h, \eta_h, \phi_h, g_h)$.

The relationship between the free energy density Ω and the on-shell action S is:

$$-\Omega V = T(S + S_\partial)_{on-shell}, \tag{S6}$$

where V is the spatial volume of the boundary system. The boundary term is given by

$$\begin{aligned}
S_\partial &= \frac{1}{2\kappa_N^2} \int_{r \rightarrow \infty} d^4x \sqrt{-h} \left[2K - 6 - \frac{1}{2}\phi(r)^2 \right. \\
&\quad \left. - \left(\frac{6c_1^4 - 1}{12} \right) \phi(r)^4 \ln[r] - b\phi(r)^4 \right. \\
&\quad \left. + \frac{1}{4}(F_{\mu\nu}F^{\mu\nu} + \hat{Z}(0)\hat{F}_{\mu\nu}\hat{F}^{\mu\nu}) \ln[r] \right].
\end{aligned} \tag{S7}$$

Here, $h_{\mu\nu}$ is the induced metric at the UV boundary with $K_{\mu\nu}$ the extrinsic curvature defined by the outward pointing normal vector to the boundary.

The boundary energy-momentum tensor reads

$$\begin{aligned}
T_{\mu\nu} &= \lim_{r \rightarrow \infty} \frac{2r^2}{\sqrt{-h}} \frac{\delta(S + S_\partial)}{\delta h^{\mu\nu}}, \\
&= \frac{1}{2\kappa_N^2} \lim_{r \rightarrow \infty} r^2 \left[2(Kh_{\mu\nu} - K_{\mu\nu} - 3h_{\mu\nu}) \right. \\
&\quad \left. - \left(\frac{1}{2}\phi^2 + \frac{6c_1^4 - 1}{12}\phi^4 \ln[r] + b\phi^4 \right) h_{\mu\nu} \right. \\
&\quad \left. - (F_{\mu\rho}F_\nu^\rho - \frac{1}{4}h_{\mu\nu}F_{\rho\lambda}F^{\rho\lambda}) \ln[r] \right. \\
&\quad \left. - \hat{Z}(0)(\hat{F}_{\mu\rho}\hat{F}_\nu^\rho - \frac{1}{4}h_{\mu\nu}\hat{F}_{\rho\lambda}\hat{F}^{\rho\lambda}) \ln[r] \right].
\end{aligned} \tag{S8}$$

Substituting the UV expansion on the boundary gives:

$$\begin{aligned}
\epsilon = T_{tt} &= \frac{(1 + 48b)\phi_s^4}{96\kappa_N^2} + \frac{\phi_s \phi_v}{2\kappa_N^2} \\
&\quad + \frac{-144f_v + 192g_4 + 12B^2 \hat{Z}[0]}{96\kappa_N^2},
\end{aligned} \tag{S9}$$

$$\begin{aligned}
p_x = p_y = T_{xx} = T_{yy} &= \frac{(3 - 48b - 8c_1^4)\phi_s^4}{96\kappa_N^2} \\
&\quad + \frac{\phi_s \phi_v}{2\kappa_N^2} + \frac{-48f_v - 8B^2 \hat{Z}[0]}{96\kappa_N^2},
\end{aligned} \tag{S10}$$

$$\begin{aligned}
-\Omega = p_z = T_{zz} &= \frac{(3 - 48b - 8c_1^4)\phi_s^4}{96\kappa_N^2} \\
&\quad + \frac{\phi_s \phi_v}{2\kappa_N^2} + \frac{-48f_v + 4(48g_4 + B^2 \hat{Z}[0])}{96\kappa_N^2}.
\end{aligned} \tag{S11}$$

Note that in the thermodynamic limit $V \rightarrow \infty$, $\Omega = -p_z$. From the EoMs (S2), we can get a radially conserved charge:

$$\begin{aligned}
Q &= e^{\frac{\eta(r)}{2}} \sqrt{g(r)} r^3 \left(r^2 \left(e^{-\frac{\eta(r)}{2}} \frac{f(r)}{r^2} \right)' - Z(\phi)A(r)A'(r) \right) \\
&\quad - B^2 \int_{r_h}^r \frac{e^{-\frac{\eta(r_s)}{2}} \sqrt{g(r_s)} \hat{Z}[\phi(r_s)]}{r_s} dr_s,
\end{aligned} \tag{S12}$$

which connects data from the horizon to the UV boundary. Evaluating it at both the horizon and the boundary yields

$$Q = Ts = \epsilon - \Omega - \mu_B n_B = \epsilon^{total} - \Omega - \mu_B n_B - BM, \tag{S13}$$

where $\epsilon^{total} = \epsilon + \epsilon^{field}$ is the total energy including the external field $\epsilon^{field} = BM$ with M the magnetization. This is the expected thermodynamic relation. More precisely, M can be computed by the partial derivative of the free energy with respect to B .

$$\begin{aligned}
M &= - \left(\frac{\partial \Omega}{\partial B} \right)_{T, \mu_B} = - \int_{r_h}^\infty \frac{B \sqrt{e^{-\eta(r)} g(r)} \hat{Z}[\phi(r)]}{r} dr \\
&\quad + \lim_{r \rightarrow \infty} \frac{B \sqrt{e^{-\eta(r)} f(r) g(r)} \ln[r] \hat{Z}[0]}{r}.
\end{aligned} \tag{S14}$$

It can be checked straightforwardly that the first law of thermodynamics

$$d\Omega = -sdT - n_B d\mu_B - MdB, \quad (\text{S15})$$

is satisfied. One can then obtain the magnetic susceptibility $\chi_B = \left(\frac{\partial M}{\partial B}\right)_{T, \mu_B}$.

Following [38], we choose $c_1 = 0.7100, c_2 = 0.0037, c_3 = 1.935, c_4 = 0.085, c_5 = 30$ of (S3). Moreover, we take $\kappa_N^2 = 2\pi(1.68), \phi_s = 1085\text{MeV}$ and $b = -0.27341$.

Appendix B: Calculation method and neural ODEs

Neural networks and neural ODEs have been intensively utilized in holographic QCD literature (e.g. [26–29]). In particular, neural networks have been effectively integrated into ODE frameworks in [27, 28]. In our approach, we introduce a novel neural ODE architecture to numerically solve the magnetic coupling $\hat{Z}[\phi(z)]$, constrained by lattice QCD data with high precision. We model \hat{Z} using a feedforward neural network with three hidden layers, each structured as $x = \sigma(\text{weight} \times x' + \text{bias})$, where the activation function is $\sigma = \tanh$. Here, x and x' represent the output and input of each layer, respectively, and $H = \{\text{weight}, \text{bias}\}$ is the parameter set. The layer structure is [input(1)-(16)-(64)-(16)-output(1)]. Details for reproducibility are provided below. Fig. 7 illustrates our computational approach. To address the inverse problem of mapping lattice QCD data to a holographic model, we initialize a trial function $\hat{Z}(\phi)$, used to solve the bulk EoMs (S2) with asymptotic AdS boundary conditions and regular horizon conditions. The solution yields boundary field theory observables, which are then compared to lattice QCD data to iteratively refine $\hat{Z}(\phi)$. Due to scaling symmetries, there are three independent IR data points: A_h, ϕ_h , and B_F , corresponding to the field values at the event horizon and a pre-scaled magnetic field. These map to the UV quantities—temperature T , chemical potential μ_B , and physical magnetic field B_T —where B_T is the transformed field after scaling. By modeling $\hat{Z}(\phi)$ through a neural network, we solve the EoMs and obtain thermodynamic quantities such as $T, \mu_B, B_T, M, s, \chi_B$, and Δp_z .

Since the lattice data [35] covers only a small region at zero chemical potential, the values of T, μ_B , and B_T computed with an arbitrary set of A_h, ϕ_h , and B_F cannot adequately cover this region. Therefore, as shown in Fig. 7, it is necessary to adjust A_h, ϕ_h , and B_F to obtain a set that effectively covers the relevant lattice QCD region. The values of the remaining thermodynamic quantities M, s, χ_B , and Δp_z depend on the choice of the trial function $\hat{Z}(\phi)$. To optimize $\hat{Z}(\phi)$, we define a loss function $L = L(M, s, \chi_B, \Delta p_z)$. We can obtain the optimal $\hat{Z}(\phi)$ by iteratively applying gradient descent (Adam: α

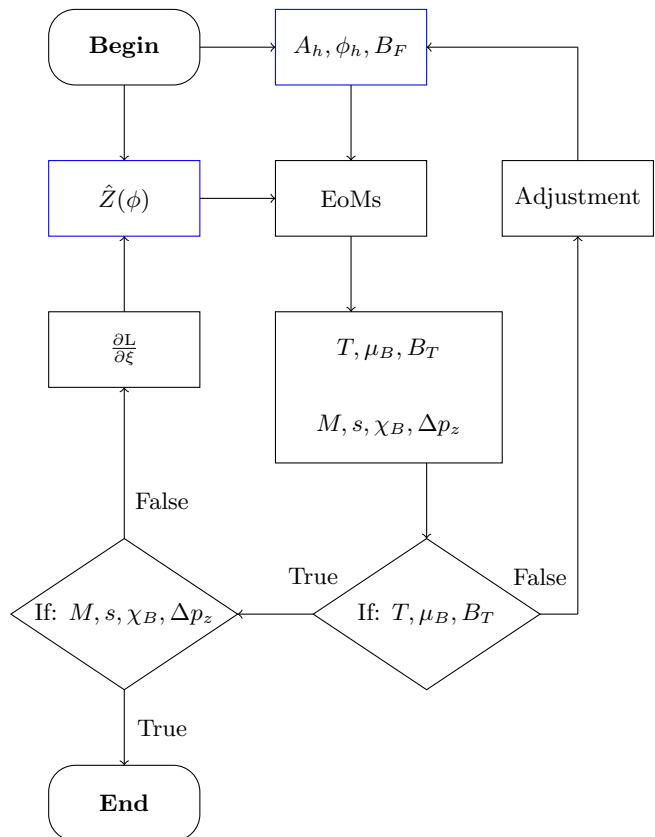


FIG. 7. Illustration of the Algorithm process: Given a trial functional $\hat{Z}(\phi)$ and a set of (A_h, ϕ_h, B_F) . Solving the EoMs (S2) to obtain the thermodynamic quantities $(T, \mu_B, B_T, M, S, \chi_B, p_z)$. Verify whether these (T, μ_B, B_T) cover the range of lattice QCD data. If not, adjust (A_h, ϕ_h, B_F) . If they do, compare this set with the corresponding lattice data for $(M, S, \chi_B, \Delta p_z)$. If consistent, terminate the process. If not, adjust $\hat{Z}(\phi)$ and repeat the process. Adjustments to $\hat{Z}(\phi)$ are made through gradient descent, where L represents the loss function and ξ are the network parameters used to mimic $\hat{Z}(\phi)$. $\frac{\partial L}{\partial \xi}$ indicates the direction of descent for the loss function. When the loss function reaches its minimum, it signifies the optimal solution for $\hat{Z}(\phi)$.

$=0.0002, \beta_1=0.9, \beta_2=0.999$) to minimize the loss function [44]. Since our model's high precision requirements, we have to employ a neural network ODE model [45] to solve for $\hat{Z}(\phi)$ throughout the entire process. This model effectively transforms the conventional neural network into a continuous form, facilitating differential equations' rapid and accurate solutions.

For later convenience, one can rephrase the EoMs (S2)

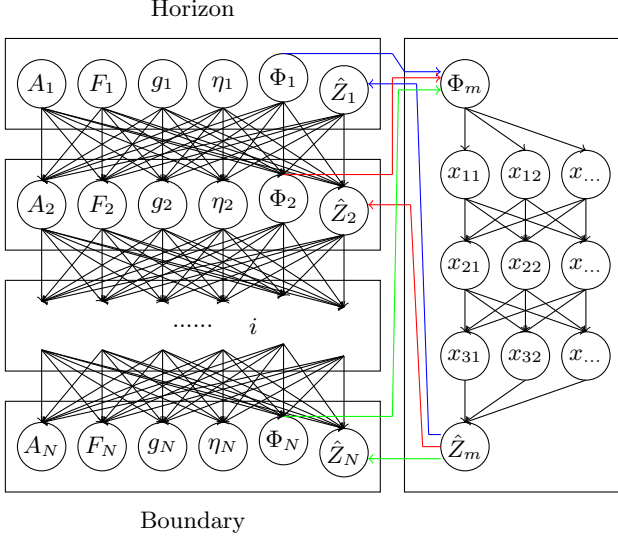


FIG. 8. Discrete network representation of the recursive relationship between layers in solving (S16). Initial conditions are set at the event horizon ($i = 1$), and layers extend to the UV boundary ($i = N$). Each layer i corresponds to field values Θ_i . The network discretizes the holographic direction z into steps dz . $\hat{Z}(\Phi)$ is modeled by a feed-forward network with three hidden layers. $\{x_{11}, x_{12}, \dots\}$ is outputs of the hidden layer. The colored arrows (e.g. green, blue, red) indicate different layers sharing the same functional form of $\hat{Z}(\Phi)$. The arrow is the forward propagation direction, and the opposite is the backpropagation direction.

as the following form:

$$\frac{d\Theta}{dz} = \Xi(z, \Theta, \dot{\Theta}(z), \hat{Z}(\Phi), \hat{Z}'(\Phi), B_F), \Theta(z) = \begin{pmatrix} \Phi(z) \\ F(z) \\ \eta(z) \\ A(z) \\ g(z) \end{pmatrix}, \quad (\text{S16})$$

where $\dot{\Theta}(z)$ is to take the derivative with respect to the argument and $z = 1/r$, $z\Phi(z) = \phi(\frac{1}{r})$, $F(z) = z^2 f(\frac{1}{r})$, $A(z) = A_t(\frac{1}{r})$, $\hat{Z}'(\Phi)$ is the derivative with respect to Φ . One can refer to the precise definitions of these functions of (S2). Ξ is a five-component vector. Θ contains scalar field ϕ , metric components f , g , η , and Maxwell field A_t . These equations of motion (S16) can be rewritten as a discrete difference equation:

$$\Theta_{i+1} = \Theta_i + \Xi(z_i, \Theta_i, \dot{\Theta}_i(z), \hat{Z}(\Phi_i), \hat{Z}'(\Phi_i), B_F) dz, \quad (\text{S17})$$

where we discretize the holographic direction z with a step size dz . The index i corresponds to the i -th layer. The equation gives the recursive relationship between the i -th layer and the $i + 1$ -th layer. Θ_i corresponds to the field value at the i -th layer. Here, $i = 1$ represents the event horizon, and $i = N$ corresponds to the UV boundary. As shown in Fig. 8, the difference equation can be naturally understood as a $6 \times N$ network without activa-

tion function.

Here, we select four thermodynamically independent data sets \mathcal{S} that contain quantities $\mathcal{S} = \{M, s, \chi_B, \Delta p_z\}$ for an accurate comparison between the holographic model and Lattice QCD data, performing a global fitting. The key problem is to minimize the loss function by optimizing the functional $\hat{Z}(\phi)$. To determine the optimizing direction of $\hat{Z}(\phi)$, one needs backpropagation of the neural network to extract the data associated with $\frac{\partial L}{\partial \xi}$. $\xi \in H$ is any parameters in \hat{Z} neural networks. And, we choose loss function $L = L(M, s, \chi_B, \Delta p_z)$ as mean-square error (MSE). Here, we apply a similar definition of the loss function offered by [46]. The precise form of loss function L is

$$L = \sum_{I \in \mathcal{S}} P_I (I_{LQCD} - I_{HQCD})^2, \quad (\text{S18})$$

where I_{LQCD} , I_{HQCD} correspond to the thermal dynamical quantities \mathcal{S} of lattice QCD data and are predicted by holographic QCD, respectively. The P_I is the inverse of the uncertainty, the maximum difference between the LQCD data and its central value.

We must input $\frac{\partial L}{\partial \xi}$ and ξ into Adam to minimize the loss function. The key issue is to collect $\frac{\partial L}{\partial \xi}$. For the i -th layer, we have the following chain rule:

$$\frac{\partial L}{\partial \xi_i} = \frac{\partial L}{\partial \Theta_{i+1}} \frac{\partial \Theta_{i+1}}{\partial \xi_i}. \quad (\text{S19})$$

Here, ξ_i is the ξ of the i -th layer, Θ_i is the Θ of the i -th layer. One has to note $\xi_i = \xi_j$, $i \neq j$ that means ξ_i in each layer are the same, but $\frac{\partial L}{\partial \xi_i} \neq \frac{\partial L}{\partial \xi_j}$. From (S17), at each layer it can be expressed by

$$\frac{\partial L}{\partial \xi_i} = \frac{\partial L}{\partial \Theta_{i+1}} \frac{\partial \Xi(z_i, \Theta_i, \hat{Z}(\Phi_i), \hat{Z}'(\Phi_i), B_F)}{\partial \xi_i} dz. \quad (\text{S20})$$

Finally, for the whole network, the key ingredient $\frac{\partial L}{\partial \xi_i}$ is the sum of all partial derivatives:

$$\frac{dL}{d\xi} = \int \frac{\partial L}{\partial \Theta} \frac{\partial \Xi}{\partial \xi} dz = \int \frac{\partial L}{\partial \Theta} \left(\frac{\partial \Xi}{\partial \hat{Z}} \frac{\partial \hat{Z}}{\partial \xi} + \frac{\partial \Xi}{\partial \hat{Z}'} \frac{\partial \hat{Z}'}{\partial \xi} \right) dz.$$

To obtain the first factor of the integrand in (S21), we can make use of the following chain rule for the two neighborhood layers:

$$\frac{\partial L}{\partial \Theta_i} = \frac{\partial L}{\partial \Theta_{i+1}} \frac{\partial \Theta_{i+1}}{\partial \Theta_i}, \quad (\text{S21})$$

where $\frac{\partial L}{\partial \Theta_i}$ represents the derivative of each component in Θ at the i -th layer, with the component index omitted for clarity. Here, $\frac{\partial \Theta_{i+1}}{\partial \Theta_i}$ is a 5×5 matrix. From (S17), we obtain:

$$\begin{aligned} \frac{\partial L}{\partial \Theta_i} &= \frac{\partial L}{\partial \Theta_{i+1}} \frac{\partial \Theta_{i+1}}{\partial \Theta_i} \\ &= \frac{\partial L}{\partial \Theta_{i+1}} \left(1 + \frac{\partial \Xi(z_i, \Theta_i, \dot{\Theta}_i(z), \hat{Z}(\Phi_i), \hat{Z}'(\Phi_i), B_F)}{\partial \Theta_i} dz \right). \end{aligned} \quad (\text{S22})$$

For convenience, let y_i denote $\frac{\partial L}{\partial \Theta_i}$, and y denote $\frac{\partial L}{\partial \Theta}$. Then, the above equation can be written as:

$$y_i = y_{i+1} \left(1 + \frac{\partial \Xi(z_i, \Theta_i, \dot{\Theta}_i, \hat{Z}(\Phi_i), \hat{Z}'(\Phi_i), B_F)}{\partial \Theta_i} dz \right), \quad (\text{S23})$$

which corresponds to the following differential form:

$$y'(z) = -y(z) \frac{\partial \Xi(z, \Theta, \dot{\Theta}(z), \hat{Z}(\Phi), \hat{Z}'(\Phi), B_F)}{\partial \Theta}. \quad (\text{S24})$$

To simplify our notations, we note that this set of equations involves five unknown functions as shown in (S16), and $\frac{\partial \Xi}{\partial \Theta}$ is a 5×5 matrix.

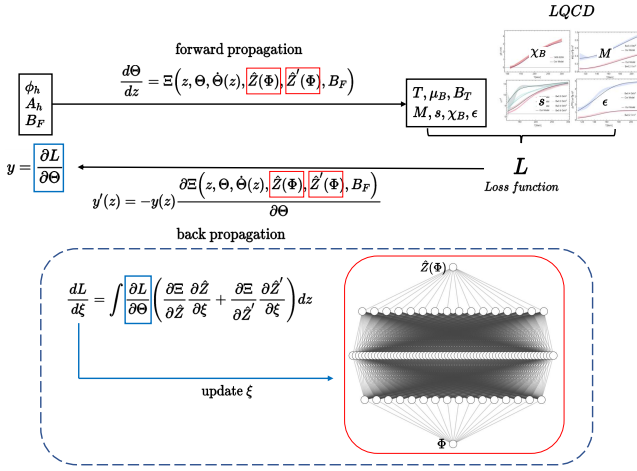


FIG. 9. Continuous representation of our numerical simulation. The top panel depicts the forward propagation, integrating from the infrared (IR, left) to the ultraviolet (UV, right), and comparing with lattice data to compute the loss function. This continuous approach corresponds to Fig. 6. During forward propagation, the function \hat{Z} acts as a numerical component within the equations of motion (EOM). The bottom panel (excluding the dashed section) illustrates backpropagation in the continuous limit. By deriving backward integral equations from the forward ones, we calculate the derivative of the loss function L with respect to the parameters ξ , subsequently updating the parameters in the $\hat{Z}(\phi)$ neural network (dashed section). Specifically, $\frac{\partial \hat{Z}}{\partial \xi}$ and $\frac{\partial \hat{Z}'}{\partial \xi}$ are obtained through the internal back propagation of \hat{Z} across the entire integration domain.

We elaborate on the forward and backpropagation for the discrete case and derive the continuous form used in practical computations. In the actual calculation, as shown in Fig. 9, we first perform a forward propagation integral to obtain the loss function, and then the derivative of the loss function with respect to the parameters can be propagated through the back differential equation, which is used for optimizing the trial function $\hat{Z}(\Phi)$ via gradient descent to minimize the loss function L . The forward and backpropagation of the \hat{Z} neural network are

respectively regarded as numerical functions participating in the forward and back differential equations.

Finally, we combine all the elements in (S21) and input them into the Adam optimizer to achieve the functional $\hat{Z}(\phi)$, which is a crucial point of this work. We managed to obtain the numerical data for $\hat{Z}(\phi)$ as shown in Fig. 2. It can be good approximated using the following analytical form:

$$\hat{Z}(\phi) = a_0 e^{-a_1(\phi-a_2)^2} + a_3 e^{-a_4(\phi-a_5)^2 - a_6(\phi-a_7)^4} + a_8 \text{sech}[-a_9(\phi-a_{10})^2] + a_{11} e^{-a_{12}(\phi-a_{13})^6} + a_{14}, \quad (\text{S25})$$

where the parameters are given by

$$\begin{aligned} a_0 &= \frac{49677}{100000}, & a_1 &= \frac{8583}{25000}, & a_2 &= \frac{202953}{100000}, \\ a_3 &= \frac{15371}{50000}, & a_4 &= \frac{6297}{50000}, & a_5 &= \frac{39131}{20000}, \\ a_6 &= \frac{411}{50000}, & a_7 &= \frac{413981}{100000}, & a_8 &= \frac{97}{4000}, \\ a_9 &= \frac{34873}{100000}, & a_{10} &= \frac{29503}{50000}, & a_{11} &= -\frac{287}{50000}, \\ a_{12} &= \frac{24319}{12500}, & a_{13} &= \frac{2637}{2500}, & a_{14} &= -\frac{691}{50000}. \end{aligned} \quad (\text{S26})$$

To illustrate the efficacy of the algorithm, we present a comparison of four thermodynamically independent quantities, $\mathcal{S} = \{M, s, \chi_B, \Delta p_z\}$, between the holographic predictions and the lattice QCD simulations, as shown in Fig.1 of the main text. Additionally, we confirm that the corresponding trace anomaly I , the renormalized longitudinal pressure Δp_z , and the renormalized anomaly ΔI predicted by the holographic model align with the lattice QCD data [35], as depicted in Fig. 10. This work represents the first quantitative realization of state-of-the-art lattice QCD data [35] within a holographic model.

* cairg@itp.ac.cn,
hesong@nbu.edu.cn,
liliphy@itp.ac.cn,
zengha20@mails.jlu.edu.cn

- [1] P. Braun-Munzinger and J. Wambach, “The Phase Diagram of Strongly-Interacting Matter,” *Rev. Mod. Phys.* **81** (2009), 1031-1050 [arXiv:0801.4256 [hep-ph]].
- [2] O. Philipsen, “The QCD equation of state from the lattice,” *Prog. Part. Nucl. Phys.* **70** (2013), 55-107 [arXiv:1207.5999 [hep-lat]].
- [3] S. Gupta, X. Luo, B. Mohanty, H. G. Ritter and N. Xu, “Scale for the Phase Diagram of Quantum Chromodynamics,” *Science* **332** (2011), 1525-1528 [arXiv:1105.3934 [hep-ph]].
- [4] J. O. Andersen, W. R. Naylor and A. Tranberg, “Phase diagram of QCD in a magnetic field: A review,” *Rev. Mod. Phys.* **88**, 025001 (2016) [arXiv:1411.7176 [hep-ph]].
- [5] Y. Aoki, G. Endrodi, Z. Fodor, S. D. Katz and K. K. Szabo, “The Order of the quantum chromodynamics transi-

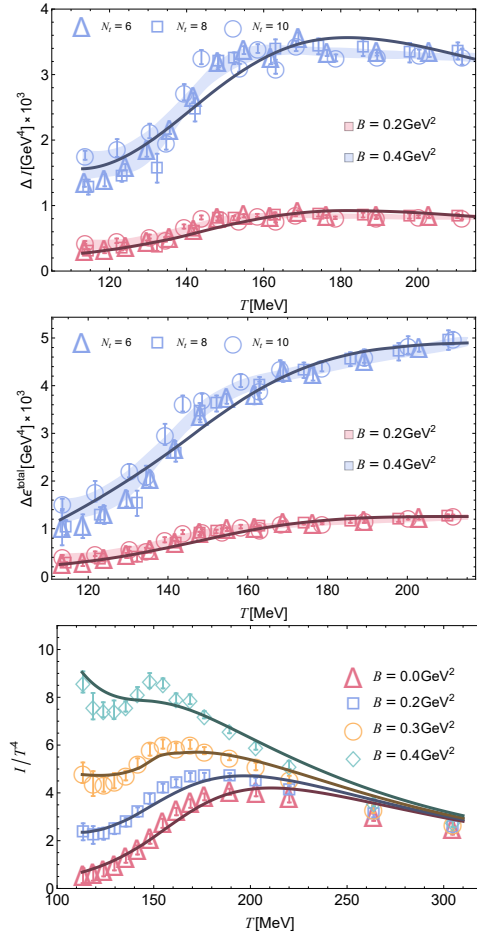


FIG. 10. The renormalized trace anomaly ΔI (top), the renormalized energy density $\Delta\epsilon = \epsilon|_B - \epsilon|_{B=0}$ (middle) and the trace anomaly I (bottom). Our holographic computations (solid curves) are compared with the latest lattice QCD results from [35]. The N_t corresponds to three lattice spacings, and B denotes the magnetic field strength. The shaded areas correspond to lattice continuum estimates.

- tion predicted by the standard model of particle physics,” *Nature* **443**, 675-678 (2006) [arXiv:hep-lat/0611014 [hep-lat]].
- [6] A. Bazavov *et al.* [HotQCD], “Chiral crossover in QCD at zero and non-zero chemical potentials,” *Phys. Lett. B* **795**, 15-21 (2019) [arXiv:1812.08235 [hep-lat]].
- [7] J. Adam *et al.* [STAR], “Nonmonotonic Energy Dependence of Net-Proton Number Fluctuations,” *Phys. Rev. Lett.* **126**, no.9, 092301 (2021) [arXiv:2001.02852 [nucl-ex]].
- [8] M. S. Abdallah *et al.* [STAR], “Measurements of Proton High Order Cumulants in $\sqrt{s_{NN}} = 3$ GeV Au+Au Collisions and Implications for the QCD Critical Point,” *Phys. Rev. Lett.* **128**, no.20, 202303 (2022) [arXiv:2112.00240 [nucl-ex]].
- [9] M. Abdulhamid *et al.* [STAR], “Beam Energy Dependence of Triton Production and Yield Ratio ($N_t \times N_p / N_d^2$) in Au+Au Collisions at RHIC,” *Phys. Rev. Lett.* **130**, 202301 (2023) [arXiv:2209.08058 [nucl-ex]].
- [10] T. Demircik, C. Ecker and M. Järvinen, “Dense and Hot

- QCD at Strong Coupling,” *Phys. Rev. X* **12** (2022) no.4, 041012 [arXiv:2112.12157 [hep-ph]].
- [11] Y. Chen, D. Li and M. Huang, “The dynamical holographic QCD method for hadron physics and QCD matter,” *Commun. Theor. Phys.* **74** (2022) no.9, 097201 [arXiv:2206.00917 [hep-ph]].
- [12] R. Rougemont, J. Grefa, M. Hippert, J. Noronha, J. Noronha-Hostler, I. Portillo and C. Ratti, “Hot QCD phase diagram from holographic Einstein–Maxwell–Dilaton models,” *Prog. Part. Nucl. Phys.* **135** (2024), 104093 [arXiv:2307.03885 [nucl-th]].
- [13] S. S. Gubser, A. Nellore, S. S. Pufu and F. D. Rocha, “Thermodynamics and bulk viscosity of approximate black hole duals to finite temperature quantum chromodynamics,” *Phys. Rev. Lett.* **101** (2008), 131601 [arXiv:0804.1950 [hep-th]].
- [14] O. DeWolfe, S. S. Gubser and C. Rosen, “A holographic critical point,” *Phys. Rev. D* **83** (2011), 086005 [arXiv:1012.1864 [hep-th]].
- [15] O. DeWolfe, S. S. Gubser and C. Rosen, “Dynamic critical phenomena at a holographic critical point,” *Phys. Rev. D* **84** (2011), 126014 [arXiv:1108.2029 [hep-th]].
- [16] U. Gursoy, M. Jarvinen and G. Nijs, “Holographic QCD in the Veneziano Limit at a Finite Magnetic Field and Chemical Potential,” *Phys. Rev. Lett.* **120** (2018) no.24, 242002 [arXiv:1707.00872 [hep-th]].
- [17] J. Grefa, J. Noronha, J. Noronha-Hostler, I. Portillo, C. Ratti and R. Rougemont, “Hot and dense quark-gluon plasma thermodynamics from holographic black holes,” *Phys. Rev. D* **104** (2021) no.3, 034002 [arXiv:2102.12042 [nucl-th]].
- [18] S. He, S. Y. Wu, Y. Yang and P. H. Yuan, “Phase Structure in a Dynamical Soft-Wall Holographic QCD Model,” *JHEP* **04** (2013), 093 [arXiv:1301.0385 [hep-th]].
- [19] T. Alho, M. Järvinen, K. Kajantie, E. Kiritsis, C. Rosen and K. Tuominen, “A holographic model for QCD in the Veneziano limit at finite temperature and density,” *JHEP* **04** (2014), 124 [erratum: *JHEP* **02** (2015), 033] [arXiv:1312.5199 [hep-ph]].
- [20] J. Knaute, R. Yaresko and B. Kämpfer, “Holographic QCD phase diagram with critical point from Einstein–Maxwell-dilaton dynamics,” *Phys. Lett. B* **778** (2018), 419-425 [arXiv:1702.06731 [hep-ph]].
- [21] R. Critelli, J. Noronha, J. Noronha-Hostler, I. Portillo, C. Ratti and R. Rougemont, “Critical point in the phase diagram of primordial quark-gluon matter from black hole physics,” *Phys. Rev. D* **96** (2017) no.9, 096026 [arXiv:1706.00455 [nucl-th]].
- [22] Y. Yang and P. H. Yuan, “QCD Phase Diagram by Holography,” [arXiv:2011.11941 [hep-th]].
- [23] R. G. Cai, S. He and D. Li, “A hQCD model and its phase diagram in Einstein–Maxwell–Dilaton system,” *JHEP* **03** (2012), 033 [arXiv:1201.0820 [hep-th]].
- [24] S. I. Finazzo, R. Critelli, R. Rougemont and J. Noronha, “Momentum transport in strongly coupled anisotropic plasmas in the presence of strong magnetic fields,” *Phys. Rev. D* **94** (2016) no.5, 054020 [arXiv:1605.06061 [hep-ph]].
- [25] K. Hashimoto, S. Sugishita, A. Tanaka and A. Tomiya, “Deep Learning and Holographic QCD,” *Phys. Rev. D* **98**, no.10, 106014 (2018) [arXiv:1809.10536 [hep-th]].
- [26] T. Akutagawa, K. Hashimoto and T. Sumimoto, “Deep Learning and AdS/QCD,” *Phys. Rev. D* **102**, no.2, 026020 (2020) [arXiv:2005.02636 [hep-th]].

- [27] K. Hashimoto, H. Y. Hu and Y. Z. You, “Neural ordinary differential equation and holographic quantum chromodynamics,” *Mach. Learn. Sci. Tech.* **2**, no.3, 035011 (2021) [arXiv:2006.00712 [hep-th]].
- [28] K. Hashimoto, K. Ohashi and T. Sumimoto, “Deriving the dilaton potential in improved holographic QCD from the chiral condensate,” *PTEP* **2023**, no.3, 033B01 (2023) [arXiv:2209.04638 [hep-th]].
- [29] X. Chen and M. Huang, “Machine learning holographic black hole from lattice QCD equation of state,” *Phys. Rev. D* **109** (2024) no.5, L051902 [arXiv:2401.06417 [hep-ph]].
- [30] In most studies, e.g. [17, 20–22], the thermodynamic variables were obtained by integrating the standard first law of thermodynamics, whose validity is still under investigation for AdS black holes with scalar hair [31–34].
- [31] L. Li, “On Thermodynamics of AdS Black Holes with Scalar Hair,” *Phys. Lett. B* **815** (2021), 136123 [arXiv:2008.05597 [gr-qc]].
- [32] T. Hertog and G. T. Horowitz, “Designer gravity and field theory effective potentials,” *Phys. Rev. Lett.* **94**, 221301 (2005) [arXiv:hep-th/0412169 [hep-th]].
- [33] A. Anabalón, D. Astefanesei, D. Choque and C. Martinez, “Trace Anomaly and Counterterms in Designer Gravity,” *JHEP* **03**, 117 (2016) [arXiv:1511.08759 [hep-th]].
- [34] H. Lu, C. N. Pope and Q. Wen, “Thermodynamics of AdS Black Holes in Einstein-Scalar Gravity,” *JHEP* **03**, 165 (2015) [arXiv:1408.1514 [hep-th]].
- [35] G. S. Bali, F. Bruckmann, G. Endrödi, S. D. Katz and A. Schäfer, “The QCD equation of state in background magnetic fields,” *JHEP* **08**, 177 (2014) [arXiv:1406.0269 [hep-lat]].
- [36] A. Bazavov *et al.* [HotQCD], “Equation of state in (2+1)-flavor QCD,” *Phys. Rev. D* **90** (2014), 094503 [arXiv:1407.6387 [hep-lat]].
- [37] S. Borsányi, Z. Fodor, J. N. Guenther, R. Kara, S. D. Katz, P. Parotto, A. Pásztor, C. Ratti and K. K. Szabó, “Lattice QCD equation of state at finite chemical potential from an alternative expansion scheme,” *Phys. Rev. Lett.* **126** (2021) no.23, 232001 [arXiv:2102.06660 [hep-lat]].
- [38] R. G. Cai, S. He, L. Li and Y. X. Wang, “Probing QCD critical point and induced gravitational wave by black hole physics,” *Phys. Rev. D* **106** (2022) no.12, L121902 [arXiv:2201.02004 [hep-th]].
- [39] Z. Li, J. Liang, S. He and L. Li, “Holographic study of higher-order baryon number susceptibilities at finite temperature and density,” *Phys. Rev. D* **108**, no.4, 046008 (2023) [arXiv:2305.13874 [hep-ph]].
- [40] F. Cuteri, “QCD thermodynamics: an overview of recent progress,” *PoS LATTICE2022* (2023), 243
- [41] As the quantitative results significantly depend on computational power, we plan to present more detailed phase structures and additional findings on the critical exponents in the forthcoming version.
- [42] K. Fukushima, B. Mohanty and N. Xu, “Little-Bang and Femto-Nova in Nucleus-Nucleus Collisions,” *AAPPS Bull.* **31**, 1 (2021) [arXiv:2009.03006 [hep-ph]].
- [43] Y. Q. Zhao, S. He, D. Hou, L. Li and Z. Li, “Phase structure and critical phenomena in two-flavor QCD by holography,” *Phys. Rev. D* **109** (2024) no.8, 086015 [arXiv:2310.13432 [hep-ph]].
- [44] Kingma, D. P., Ba, J., “Adam: A method for stochastic optimization,” [arXiv:1412.6980].
- [45] R. T. Q. Chen, Y. Rubanova, J. Bettencourt, and D. K. Duvenaud, “Neural Ordinary Differential Equations,” *Advances in Neural Information Processing Systems*, vol. 31, 2018.
- [46] S. Shi, L. Wang and K. Zhou, “Rethinking the ill-posedness of the spectral function reconstruction — Why is it fundamentally hard and how Artificial Neural Networks can help,” *Comput. Phys. Commun.* **282**, 108547 (2023) [arXiv:2201.02564 [hep-ph]].